IEEE Access
Multidisciplinary | Rapid Review | Open Access Journal

Received October 6, 2018, accepted November 2, 2018, date of publication November 14, 2018,
date of current version December 19, 2018.

Digital Object Identifier 10.1109/ACCESS.2018.2881212

Direct-Drive Conical-Rotor Permanent Magnet Synchronous Generator for Turbo-Expander, Accounting for Adaptive Equilibrium of Axial Force

JIAOBAO WANG, SHOUDAO HUANG, (Senior Member, IEEE), CHAO GUO, HAOKUN WU, AND YAOJING FENG

College of Electrical and Information Engineering, Hunan University, Changsha 410082, China

Corresponding author: Yaojing Feng (e-mail: fengyaojing@hnu.edu.cn)

This work was supported in part by the National Natural Science Foundation of China under Grant 51737004 and Grant 51407064 and in part by the Natural Science Foundation of Hunan Province, China, under Grant 2018JJ2044.

ABSTRACT The permanent magnet synchronous generator (PMSG) has been widely employed in high-speed direct-drive turbo-expander for distributed energy generation. However, for conventional PMSG based turbo-expander system, expensive mechanical balance devices should be installed on the rotor to restrain the axial force of turbine impeller under high-speed flow, which may cause both complex system structure and higher manufacturing cost. Thus, in this paper, a direct-drive conical-rotor PMSG (CR-PMSG) for turbo-expander is developed, which can generate an axial magnetic force as equilibrant to counteract the axial force of turbine impeller without mechanical balance device, so as to reduce the system complexity, improve the operating performance and extend the operating cycle. First, the structural features of the CR-PMSG are introduced and the basic principle of axial force balance is analyzed. Then, a 1.5 kW, 6000 rpm CR-PMSG with cone angle of 6° is designed. Using 3-D finite element analysis, the axial force of turbine impeller, the axial magnetic force of the rotor, and the electromagnetic performance are simulated. Also, the control strategy of d, q-axis currents is obtained to achieve the adaptive equilibrium of axial force. Finally, a CR-PMSG prototype is fabricated and tested to validate the theory.

INDEX TERMS Adaptive equilibrium of axial force, conical-rotor permanent magnet synchronous generator (CR-PMSG), finite element analysis (FEA), turbo-expander.

I. INTRODUCTION

The PMSG based high-speed direct-drive turbo-expander has been widely accepted as a good alternative in small energy recycling power generation, especially in distributed energy turbine generation systems, such as low temperature waste-heat and geothermal generation system based on Organic Rankine cycle (ORC), downhole generator system, gas generation system of power stations and energy recovery system of engine power turbine [1]–[7]. However, to ensure a safe and reliable operation of the system, the axial force of turbine impeller under the impact of high-speed working-fluid flow (could be as large as 150 N for a 1.6 kW, 6000 rpm small turbo-expander, and 3100 N for a 350 kW, 8000 rpm large turbo-expander) should be balanced usually by mechanical devices such as compression spring, balance plate, slider and special bearings. Moreover, the axial force changes aperiodically due to the influence of temperature, pressure and flow of the working-fluid, so the impeller blades will collide with the volute for vibration and friction, causing abnormal wear and tear of the bearings, balance plate and spring. As a result, not only the axial force should be calculated accurately, but also the balanced device should be designed and selected accurately, which significantly increases the manufacturing cost and design complexity. Practically, this traditional method cannot obtain a suitable balancing result. Thus, some mitigation solutions have been proposed and investigated in recent years.

In [8] and [9], special bearings are used in the balance system for suppression the axial force of turbine impeller. The studies show that the evaluation of the axial force at

different conditions is essential for a reliable bearing design and stable operation. To assure the bearing's long-term and reliable operation, the axial force on the thrust ball bearing of the rotor should be first measured under actual operating conditions, and then be adjusted to a predetermined range with a predetermined method. by using this method, the adjusting workload of axial force can be reduced significantly, but a large number of complex theoretical analysis and engineering practice are needed to ensure the accuracy.

In [10] and [11], a novel double-turbine structure is proposed. Two identical turbo-expanders are symmetrically mounted on one generator, and the axial forces of impeller at the two sides can be counteracted with each other. This structure can improve the electro-mechanical conversion efficiency and suppresses axial force, but the system cost is much higher, and the control algorithm is relatively complex.

Similar issue can also be found in other type of flow turbines such as the turbomachinery, turbopump and turbocharger, etc. [12]–[14]. The common problem is the inability of the balancing device to quickly and adaptively suppress axial forces under variable conditions, which results in shorter operating cycle.

Therefore, it becomes urgent to find a simpler but more effective method for counteracting the axial force of turbine impeller to solve the above problems. To provide a probable solution, a conical-rotor (CR) PMSG for high-speed direct-drive turbo-expander has been developed in this paper. Due to its conical-rotor shape, the CR-PMSG can adaptively generate an axial magnetic force as equilibrant to counteract the axial force of turbine impeller. As a result, only a conventional bearing will be used to support the shaft, thus avoiding the use of complex spring-bearing system or an expensive symmetrical double-turbine drive structure.

At present, studies on conical-rotor machines are mainly focused on the structure design and performance analysis. Reference [15] introduces a novel motor that consists of two conical air gap bearingless PM half-motors, mounted on a single shaft, and a 1 kW, 18000 rpm prototype has been designed and built. Reference [16] studies the flux weakening performance of a conical-rotor PMSM, which has a special conical-rotor that can be moved outside in axial direction, and a prototype machine is designed and built to validate the theory. As there is almost no precedent for the use of conical-rotor machine in the turbo-expander, the study in this paper may provide a theoretical guidance for the application of CR-PMSG in turbomachinery. The structure features are discussed, and the basic balance principle of the axial force and adaptive equilibrium is analyzed. A 1.5 kW, 6000 rpm CR-PMSG is designed and simulated. By using 3-D finite element method (FEM), the investigation focuses on the axial force of turbine impeller and the axial magnetic force of the CR-PMSG to obtain the current control strategy for adaptive equilibrium. A prototype is then fabricated and tested to validate the theoretical design and analysis.

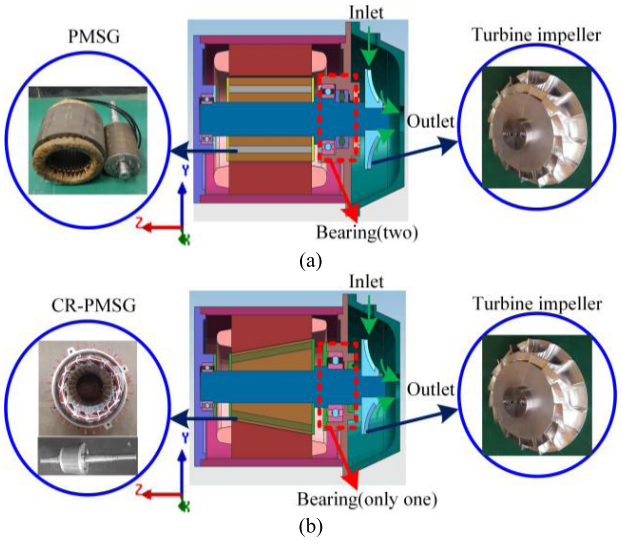

FIGURE 1. Basic structure of the high-speed direct-drive turbo-expander: (a) conventional PMSG based. (b) CR-PMSG based.

II. THEORETICAL ANALYSIS OF AXIAL FORCE

A. STRUCTURE OF THE CR-PMSG FOR TURBO-EXPANDER

For the high-speed direct-drive turbo-expander system, the PMSG is usually coaxially connected to a turbine impeller, as shown in Fig. 1. When the system works, the high-speed working-fluid flows into the turbine through radial inlet to rotate the impeller, and then goes through the axial outlet; the PMSG rotates following the impeller, converting mechanical energy into electricity power. At the same time, the pressure difference between the inlet and outlet of turbine will produce an axial force $F_{\mathrm{exp},-\mathrm{Z}}$ (negative direction of Z axis).

It can be seen from Fig. 1(a) that besides the support bearing, the conventional PMSG for turbo-expander needs a thrust bearing to counteract the axial force of turbine impeller, by which the system cost and difficulty in manufacturing will be significantly increased. While the proposed CR-PMSG features a conical-rotor structure, as shown in Fig.1(b), which can generate an axial magnetic force $F_{\mathrm{gen,Z}}$ (positive direction of Z axis) to counteract the axial force of turbine impeller, so the thrust bearing can be reduced to simplify the system structure.

B. THE AXIAL FORCE OF TURBINE IMPELLER

Turbine impeller is one of the key components which can convert heat energy to revolving mechanism kinetic energy. According to the basic principles of Engineering Physics, the total output power W_{exp} and torque T_{exp} of turbine impeller can be expressed as follows

$$\begin{cases} W_{\mathrm{exp}} = q_{\mathrm{m}} \Delta h_{\mathrm{s}} \eta_{\mathrm{exp}} = q_{\mathrm{m}} C_{\mathrm{p}} T_{\theta} (1 - \dfrac{1}{\tau^{(k-1)/k}}) \eta_{\mathrm{exp}} \\ T_{\mathrm{exp}} = 30 \times \dfrac{W_{\mathrm{exp}}}{\pi n} \end{cases} \quad (1)$$

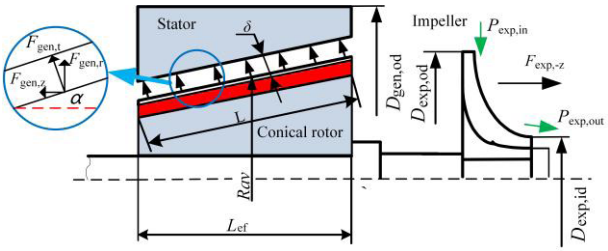

FIGURE 2. Axial section of the CR-PMSG based direct-drive turbo-expander.

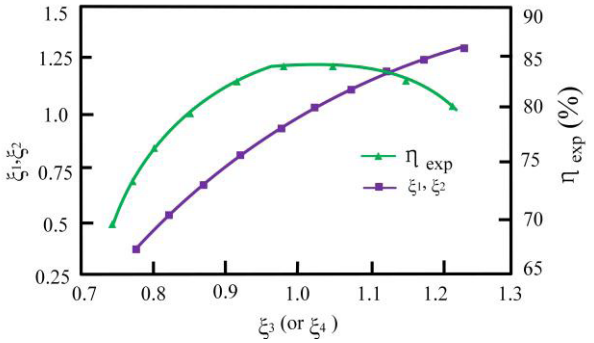

FIGURE 3. Axial force characteristics and system efficiency under various working conditions.

where, q_m, Δh_s, η_{exp}, C_p, T_θ, τ, k and n are the fluid flow, isentropic enthalpy, turbine efficiency, isobaric heat capacity, inlet temperature, expansion ratio, heat capacity ratio and speed, respectively.

Fig. 2 shows an axial section of the CR-PMSG based direct-drive turbo-expander. The axial force of turbine impeller, which is caused by the pressure difference between the inlet and outlet, can be calculated by (2), according to the thermal and dynamic analysis [2], [17]

$$\begin{aligned} F_{exp,-Z} &\cong \frac{\pi}{4}(D_{exp,od}^2 - D_{exp,id}^2)P_{exp,in} \\ &\quad - \frac{\pi}{4}(D_{exp,od}^2 - D_{exp,id}^2)P_{exp,out} \\ &= \frac{\pi}{4}(P_{exp,in} - P_{exp,out})(D_{exp,od}^2 - D_{exp,id}^2) \end{aligned} \tag{2}$$

where, $D_{exp,od}$ and $D_{exp,id}$ are the outer and inner diameters of impeller, $P_{exp,in}$ and $P_{exp,out}$ are the inlet and outlet pressures.

According to (2), once the geometry of impeller has been determined, the larger the expansion ratio $\tau = P_{exp,in}/P_{exp,out}$ is, the larger axial force would be. Therefore, the key parameters such as expansion ratio, inner diameter and outer diameter of the turbine impeller should be fully considered in the design to adjust the axial force, and the balance devices should be selected and designed reasonably. In order to facilitate the analysis, assuming that W_{expr}, $F_{exp,-Zr}$, $P_{exp,inr}$ and τ_r are respectively the rated values of W_{exp}, $F_{exp,-Z}$, $P_{exp,in}$ and τ, and define ratio values $\xi_1 = W_{exp}/W_{expr}$, $\xi_2 = F_{exp,-Z}/F_{exp,-Zr}$, $\xi_3 = P_{exp,in}/P_{exp,inr}$, $\xi_4 = \tau/\tau_r$.

The axial force characteristics, as well as the system efficiency are analyzed under various working conditions and depicted in Fig. 3 [18]. These curves are obtained by empirical experiments performed on turbines, then the axial force of turbine impeller can be determined from its expansion ratio accordingly. From Fig. 3, the increasing inlet pressure results in an increase of axial force, and the system efficiency η_{exp} reaches a peak value when $\xi_3 \approx 1$ (or $\xi_4 = 1$).

C. THE AXIAL MAGNETIC FORCE OF THE CR-PMSG

The stator winding structure of the CR-PMSG is the same as the conventional PMSG. However, the two ends of the conical-rotor have different diameters, and both the yoke height and tooth width along the axial direction change with the rotor diameter linearly [15], [19]. In Fig. 2, define L_{ef} and R_{av} as the length of iron core and the average radius of rotor, respectively.

The air gap magnetic field is synthesized by PM magnetic field and armature reaction magnetic field if the saturation is not considered. According to the double reaction theory of synchronous motor, armature reaction can be equivalent to the superposition of the effect of the d-axis and the q-axis component [20].

Thus, the air gap flux density B_δ can be equivalent to the superposition of the PM flux density and the d, q-axis armature reaction flux densities generated by d, q-axis currents, which expressed as

$$B_\delta(\theta, Z) = B_0(\theta, Z) + B_{1d}(\theta, Z) + B_{1q}(\theta, Z) \tag{3}$$

where, B_0, B_{1d}, B_{1q}, θ and Z are the PM flux density, the d-axis armature reaction flux density, the q-axis armature reaction flux density, the circumferential angle and the axial position of the rotor, respectively.

At a fixed axial position, the specific expressions of the flux densities are as follows

$$\begin{cases} B_0(\theta) = \dfrac{B_r h_m}{h_m + \mu_0 \delta} \sin(p\theta) \\ B_{1d}(\theta) = \dfrac{3\mu_0 N_s}{\pi \delta} I_d K_{dp} F_{1d} \sin(p\theta) \\ B_{1q}(\theta) = \dfrac{3\mu_0 N_s}{\pi \delta} I_q K_{dp} F_{1q} \sin(p\theta + \dfrac{\pi}{2}) \end{cases} \tag{4}$$

where, μ_0 is the permeability of vacuum ($\mu_0 = 4\pi \times 10^{-7}$H/m); B_r, h_m, and δ are the PM remanence, the PM thickness (length of the magnetization direction) and the air gap length, respectively; K_{dp}, N_s, I_d, I_q, F_{1d}, F_{1q} and p are the winding coefficient, turn numbers per phase, d-axis current, q-axis current, d-axis magnetic potential,q-axis magnetic potential, and pole pairs, respectively.

From (4), B_{1d} is of the same or reversed phase as B_0, enhancing or weakening the magnetic field. While,B_{1q} is in the orthogonal phase of B_0, enhancing the magnetic field and causing waveform change.

In general, the axial magnetic force can be calculated by the virtual displacement method [15], [21] or the Maxwell stress tensor method [22]. The latter is employed in this paper for

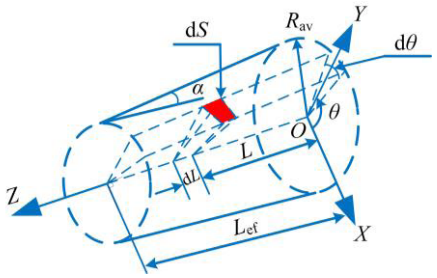

FIGURE 4. Structure parameters and geometric coordinate of the conical-rotor.

investigating the magnetic force, and the force components per air gap area element can be determined by

$$\vec{f} = \begin{bmatrix} f_{\text{gen,r}} \\ f_{\text{gen,t}} \\ f_{\text{gen,Z}} \end{bmatrix} = \frac{1}{2\mu_0} \begin{bmatrix} \left(B_{\delta n}^2 - B_{\delta t}^2\right)\cos\alpha \\ 2B_{\delta n}B_{\delta t} \\ \left(B_{\delta n}^2 - B_{\delta t}^2\right)\sin\alpha \end{bmatrix} \tag{5}$$

where, $f_{\text{gen,r}}$, $f_{\text{gen,t}}$ and $f_{\text{gen,Z}}$ are respectively the radial, tangential and axial component of the force, of which $f_{\text{gen,r}}$ and $f_{\text{gen,Z}}$ compose to the normal component; $B_{\delta n}$ and $B_{\delta t}$ are the normal and tangential component of the air gap flux density; α is the cone angle of the rotor.

As can be seen from Fig. 4, the unit area dS on the rotor surface can be modeled and analyzed by

$$\mathrm{d}S = \int_0^{2\pi} \int_{-L_{\text{ef}}/2}^{L_{\text{ef}}/2} (R_{\text{av}} - L\tan\alpha)\sin\alpha\tan\alpha \mathrm{d}\theta \tag{6}$$

In a low saturated PM machine, the flux lines in the air gap are nearly perpendicular to the outer surface of the rotor, which implies that $B_{\delta t} \ll B_{\delta n}$, so the force densities could be further simplified to

$$\vec{f} = \begin{bmatrix} f_{\text{gen,r}} \\ f_{\text{gen,t}} \\ f_{\text{gen,Z}} \end{bmatrix} \cong \frac{1}{2\mu_0} \begin{bmatrix} B_{\delta n}^2\cos\alpha \\ 2B_{\delta n}B_{\delta t} \\ B_{\delta n}^2\sin\alpha \end{bmatrix} \tag{7}$$

Substituting (3), (4) and (6) into (7), yields

$$F_{\text{gen,Z}} = \frac{1}{2\mu_0} \int \left[\dot{B}_0 + \dot{B}_{1\text{d}} + \dot{B}_{1\text{q}}\right]^2 \sin\alpha \mathrm{d}S \tag{8}$$

Terms with '·' on head in (8) mean that they are vector quantities. Usually the armature reaction magnetic field is smaller than the permanent magnetic field, and the main influence on B_δ is $B_{1\text{d}}$. So, (8) could be approximately simplified to be [15] [23]

$$F_{\text{gen,Z}} \approx \frac{1}{2\mu_0} \int \left[\dot{B}_0 + \dot{B}_{1\text{d}}\right]^2 \sin\alpha \mathrm{d}S \tag{9}$$

This can be verified by finite element analysis (FEA) as shown in Fig. 16(a) of Section III, Part C in this paper. But of course, if the q-axis current is large, the influence of q-axis armature reaction flux on the air gap magnetic field cannot be ignored. It is difficult to analyze the influence and there is no accurate analytical calculation method for the$q$-axis armature reaction magnetic field at present, then the calculation results of $F_{\text{gen,Z}}$ need to be corrected by electromagnetic field simulation analysis.

According to (8) and (9), once the CR-PMSG rotates, an axial magnetic force will be produced, and it will change with the stator current.

In conclusion, the axial magnetic force, no-load back EMF and electromagnetic torque are mainly relevant to the air gap magnetic field, air gap length, outer diameter of the conical-rotor, core length, cone angle, etc. [24], [25]. From (3) and (9), once the geometry of the CR-PMSG is fixed, the axial force $F_{\text{gen,Z}}$ can be magnetically enhanced ($i_{\text{d}} > 0$) or weakened ($i_{\text{d}} < 0$) by changing the amplitudes of the d, q-axis currents.

For salient-pole generators, the output power and torque (absolute value for the generator) can be calculated as follows [26]

$$\begin{cases} W_{\text{gen}} = m(ui_{\text{q}}\sin\beta + ui_{\text{d}}\cos\beta)\eta_{\text{gen}} \\ T_{\text{gen}} = p\left[\psi_{\text{pm}}i_{\text{q}} + (L_{\text{d}} + L_{\text{q}})i_{\text{d}}\right] \end{cases} \tag{10}$$

where, m, u, β, p, ψ_{pm}, L_{d}, L_{q} and η_{gen} respectively denote the phase number, voltage amplitude, power angle, pole-pair number, PM flux linkage, d-axis inductance, q-axis inductance and the generator efficiency.

According to (4), (9), (10), the air gap magnetic field is affected by the$d$, q-axis currents. When the air gap magnetic density amplitude is constant, the axial force will be larger if the d-axis current component is large, and the power will be larger if the q-axis current component is large. The analysis of B_δ will be necessary for the calculation of $F_{\text{gen,Z}}$.

D. ADAPTIVE EQUILIBRIUM OF AXIAL FORCE

According to (1), (2), (9), (10) and Fig. 3, the output power of the CR-PMSGW_{gen} and adaptive equilibrium of axial force can be expressed as

$$\begin{cases} W_{\text{gen}} = W_{\text{exp}}\eta_{\text{gen}} \propto f(P_{\text{exp,in}}, T_{\text{gen}}) \propto f(P_{\text{exp,in}}, i_q) \\ F_{\text{gen,Z}} = F_{\text{exp,-Z}} \propto f(P_{\text{exp,in}}, B_\delta) \propto f(P_{\text{exp,in}}, i_d) \end{cases} \tag{11}$$

with no-load losses neglected, $T_{\text{exp}} = T_{\text{gen}}$ can be considered.

From (11), the output power W_{gen} corresponds to a certain inlet pressure $P_{\text{exp,in}}$ (or expansion ratio τ) and torque T_{gen} (or i_{q}); the axial force corresponds to a certain inlet pressure $P_{\text{exp,in}}$ (or expansion ratio τ) and i_{d}. So, when the turbine speed is constant, the pressure (or flow) at the turbine inlet and the q-axis current i_{q} of the generator have the greatest influence on the output power; while the d-axis current of the generator plays a dominant role in suppressing the axial force change of the turbine.

III. 3-D FEA OF CR-PMSG AND TURO-EXPANDER

Based on the above analysis of axial force and according to the design method of PM machines, a CR-PMSG prototype is designed, and the main geometry and electrical parameters are provided in Table 1.

A. 3-D MODELING OF TURBO-EXPANDER

For simplification, we assume that the volume between components is negligible, and the input flow ($q_{\text{m-in}}$) equals the

TABLE 1. Main design parameters of the CR-PMSG prototype.

Parameter	Symbol	Value
Rated power	W_{gen}	1.5 kW
Rated speed	n_N	6000 rpm
Pole pairs	p	2
Working medium	-	compressed air
Expansion ratio	τ	2.5
Outer diameter of the stator	$D_{gen,od}$	167 mm
Air gap length	δ	0.7 mm
Average outer diameter of the rotor	$D_{gen,in}$	105.5 mm
Axial core length	L_{ef}	52 mm
Cone angle	α	6°
Stator resistance	R	1.002 Ω
d-axis inductance	L_d	10.94 mH
q-axis inductance	L_q	20.49 mH
Flux per pole	ψ	0.334 Wb
No-load back EMF	E_0	242 V
Estimated rotor inertia	J	0.00344 kg m^2

TABLE 2. Main geometry and performance parameters of the turbo-expander.

Parameter	Symbol	Value
Outer diameter	$D_{exp,od}$	190 mm
Inner diameter	$D_{exp,in}$	165 mm
Blade thickness	H	20 mm
Rated inlet pressure	$P_{exp,in}$	121.6 kPa
Rated outlet pressure	$P_{exp,out}$	95 kPa
Inlet temperature	T_θ	308 K
Inlet flow	q_m	600 Nm^3/h

output flow (q_{m-out}) at any time instant [27].

$$\dot{q}_{m-in} \approx \dot{q}_{m-out} \tag{12}$$

The 3-D model of the designed turbine impeller is built, as shown in Fig. 5, of which the main geometry and operation parameters are listed in Table 2. During the analysis, only the force on impeller blades (see Fig. 6) is calculated, and Fig. 7 shows the pressure distribution of impeller blades with the inlet pressure varying from 106 kPa to 160.5 kPa.

By FE simulation, the output power (and axial force) varies with the inlet pressure can be obtained, as depicted in Fig. 8. It can be seen that the output power W_{exp} is 1.6 kW and the axial force $F_{exp,-Z}$ is 150 N at the rated design point. Furthermore, the output power and axial force are almost linear with the inlet pressure.

B. 3-D MODELING AND ANALYSIS OF THE CR-PMSG

The axial magnetic tensile can be obtained by the FE method when the armature winding is with different$d$, q-axis currents [24], [28]. In order to simplify the calculation, a quarter

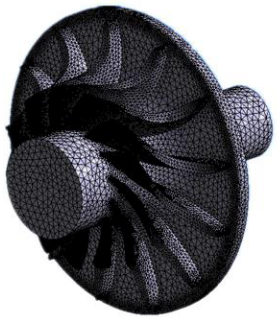

FIGURE 5. 3-D FE model of the turbine impeller.

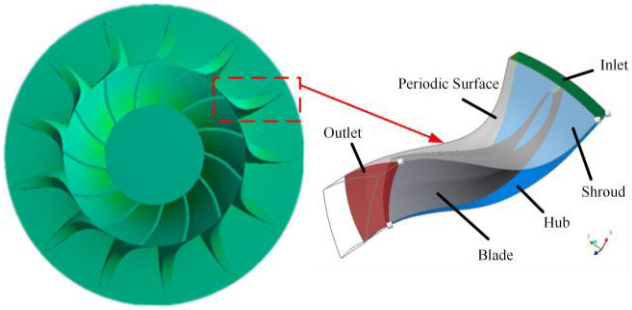

FIGURE 6. The impeller blade area for axial force analysis.

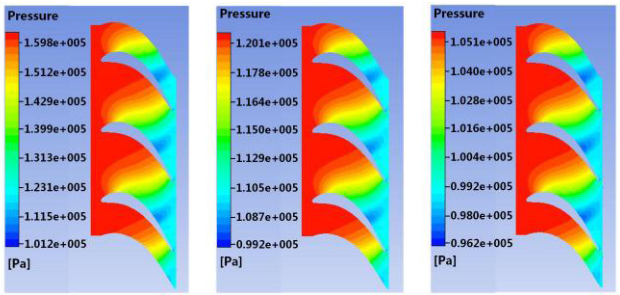

FIGURE 7. Pressure distribution of impeller blades with different inlet pressures: (a) Inlet pressure of 121.6kPa; (b) Inlet pressure of 160.5 kPa; (c) Inlet pressure of 106.2kPa.

of the 3-D model is established from the symmetrical construction, as shown in Fig. 9.

The flux density distribution of CR-PMSG is shown in Fig. 10. It can be seen that because of unequal length of stator yoke height, the flux density distribution at the two ends of stator iron core is not uniform, while a similar flux density distribution can also be found in the rotor yoke. Besides, since the slot height is constant, the tooth height will also be constant, while the tooth width changes very little along the axis. So, the flux density distribution of the stator teeth is almost uniform.

In the proposed CR-PMSG, the salient rotor structure features rectangular PMs and uniform air gap. As can be seen from Fig. 4, L represents the axial coordinate and θ represents the circumference coordinate.

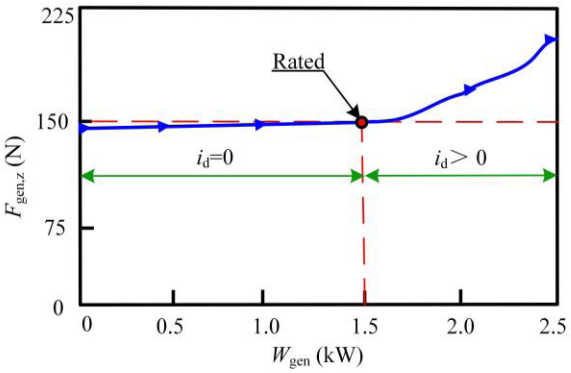

FIGURE 8. Output performance of the turbine with respect to inlet pressure.

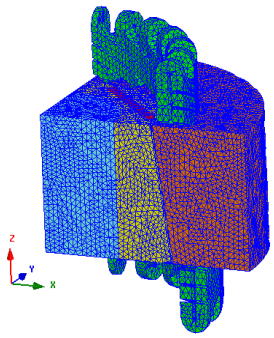

FIGURE 9. A quarter of 3-D FE CR-PMSG model.

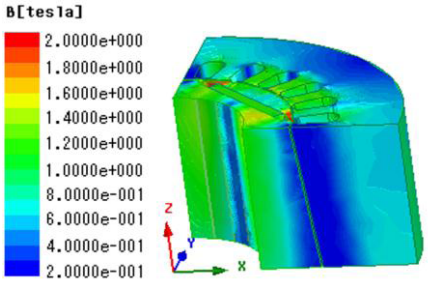

FIGURE 10. Flux density distribution of the CR-PMSG.

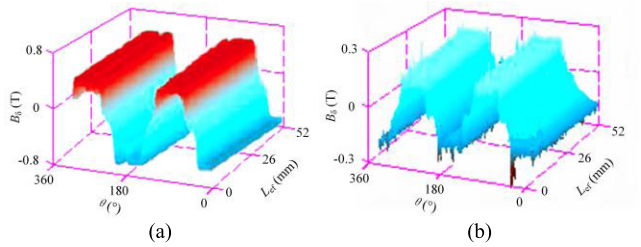

FIGURE 11. Air gap flux density at no load: (a) Radial distribution; (b) Axial distribution.

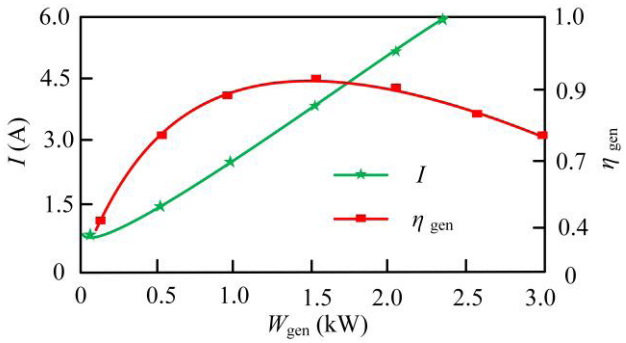

FIGURE 12. Simulated power and axial force curves.

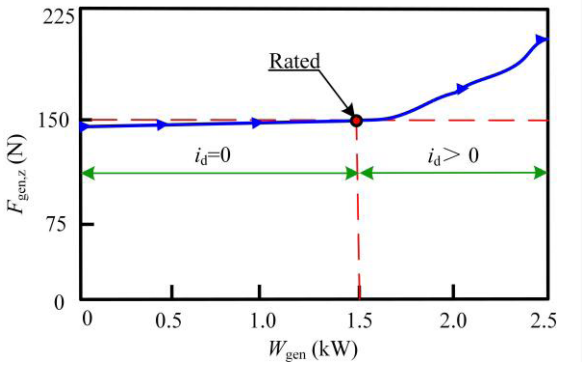

FIGURE 13. Simulated axial force curve under *d*-axis current.

Then the distribution of the air gap magnetic field can be obtained by FE analysis, as shown in Fig. 11. It can be seen that both axial and radial flux densities have a sinusoidal but flat-top distribution. Besides, both waveforms have a 90° phase difference between each other. It is also noteworthy that because of small amplitude of axial air gap flux density and nonideal precision of FE subdivision, some spikes/disturbances are brought into the results.

Fig. 12 shows the operation curve of the CR-PMSG. Affected by magnetic saturation, the output power increases slowly with the increase of current. The maximum efficiency is about 93.1%.

The simulated axial force curve is descripted in Figure 13, which shows that the axial force increases with the increase of *d*-axis current i_d.

C. INTEGRATED SYSTEM ANALYSIS OF THE CR-PMSG DIRECT-DRIVEN TURBO-EXPANDER

In order to achieve an adaptive equilibrium of axial force by control, based on the established 3D model, the working characteristics of the turbine are simulated, and the turbine-generator-controller integrated system is analyzed. To reduce the failure rate, sensorless rotor position detection method is applied. The axial force and output power double closed-loop control system is proposed and depicted in Fig. 14.

Firstly, the parameters of turbine inlet, such as temperature, pressure and flow rate, etc., are measured, the reference power W_{exp} and axial force $F_{exp,-Z}$ are calculated according to (1) and (2).

Next, the difference between the calculated axial force $F_{exp,-Z}$ and the measured axial force F_a on the coaxial shaft, as well as the corresponding *d*-axis current i_d, is fed into

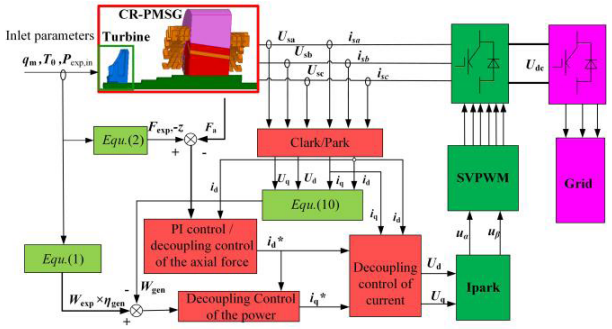

FIGURE 14. Control schematic diagram for adaptive equilibrium of axial force.

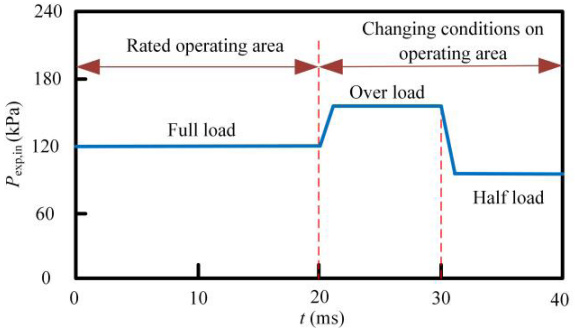

FIGURE 15. The inlet pressure variation of the turbo-expender for tests.

the controller. The controller judges whether the magnetic field is saturated and sets different control parameters, so as to get the reference value of the d-axis current (i_d^*). When the magnetic field is unsaturated, PI control for the linear working area is designed in accordance with the system requirements; when the magnetic field is saturated, the nonlinear decoupling control is adopted. The specific methods are as follows: $i_d = 0$ control is used for light load and rated load;$i_d > 0$ control is used for overload; i_d is adjusted until the axial force difference is close to zero. At the same time, the current i_d is sent to the power controller.

In the power loop, the difference between the calculated output power W_{exp} and the measured output power W_{gen} of the CR-PMSG is fed into the controller, and then the d-axis current i_d obtained from the axial force loop is combined to output the d, q-axis currents, which are sent to the current decoupling controller and converted to voltage signals for the SVPWM generator. After rectification, the generator is connected to the grid.

According to the simulation curves of axial force and power of turbine and generator, change the inlet pressure to adapt different load conditions. The inlet pressure variation of the turbo-expender is in accordance with the command curve shown in Fig. 15, of which the inlet pressure should be set to adapt to 100% (full load), 170% (over load), and 50% (half load) of rated load at $t = 0$, 20ms, 30ms, respectively.

A prediction of axial force and torque with respect to d, q-axis currents are obtained by FE method, as shown

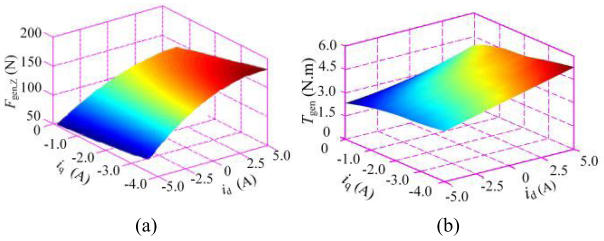

FIGURE 16. Prediction with respect to *d, q*-axis currents: (a) Axial force; (b) Electromagnetic torque.

in Fig. 16. The axial magnetic force has a quite slight increase with the increase of q-axis current from Fig. 16(a), which confirms the previous analysis and conclusion in (8) and (9). This prediction result is similar to the research conclusion presented in [29]–[31]. While, as the d-axis current increases, the axial force will increase significantly. Also, in combination with Fig. 8 and Fig. 16(a), when the axial magnetic force reaches the rated value of 150N at the inlet pressure of 121.6kPa, the FE predicted current is about $i_d = 0$ and $i_q = -3$ A. Besides, it can be seen from Fig. 16(b) that the torque will increase as the q-axis current increases, which is consistent with the operation theory of synchronous generator. The maximum predicted torque ($T_{gen,max}$) is about 5.1 N.m.

For better comparison with the experimental performance, more simulation results such as output power, currents (including d-axis and q-axis current components), axial force of the shaft system, etc., are presented in Section IV.

IV. EXPERIMENTAL VALIDATION AND ANALYSIS

A. CONFIGURATION OF THE PROTOTYPE TEST

In order to evaluate the performance of the proposed CR-PMSG based turbo-expander, a prototype was fabricated and tested.

The compressed air is used to push the turbine impeller to rotate. As shown in Fig. 17, the parameters that can be adjusted on experimental platform are the flow rate and the pressure of compressed air. The inlet of the turbo-expander is connected to the air source, and the flow rate of compressed air into the turbo-expander can be controlled by adjusting the valve. The inlet pipeline is equipped with a thermal resistance, pressure gauge and mass flowmeter to measure the temperature and flow parameters of the turbo-expander air at the inlet. While, the outlet pipeline is equipped with a thermal resistance and pressure gauge to measure the temperature and pressure of the exhaust air. Turbo-expander is directly connected to the shaft of the CR-PMSG, driven by a special converter, and the other end of the CR-PMSG shaft is equipped with an axial force measure device.

The whole prototype test rig is shown in Fig. 18, which is composed of a CR-PMSG prototype, an oscilloscope, a turbo-expander, a volute and a controller. Firstly, the compressed air is injected into the volute and then expanded to push the turbine impeller. So, the turbo-expander starts to rotate, and

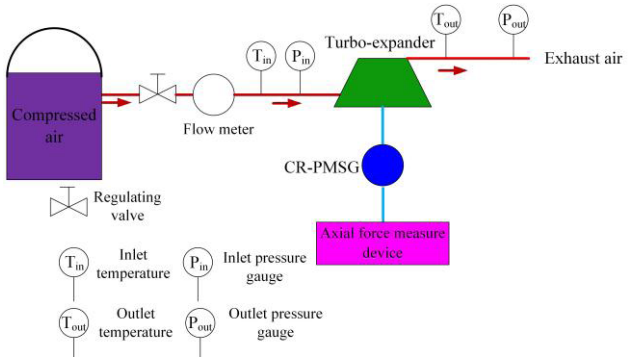

FIGURE 17. Performance test flowchart of CR-PMSG direct-driven turbo-expander.

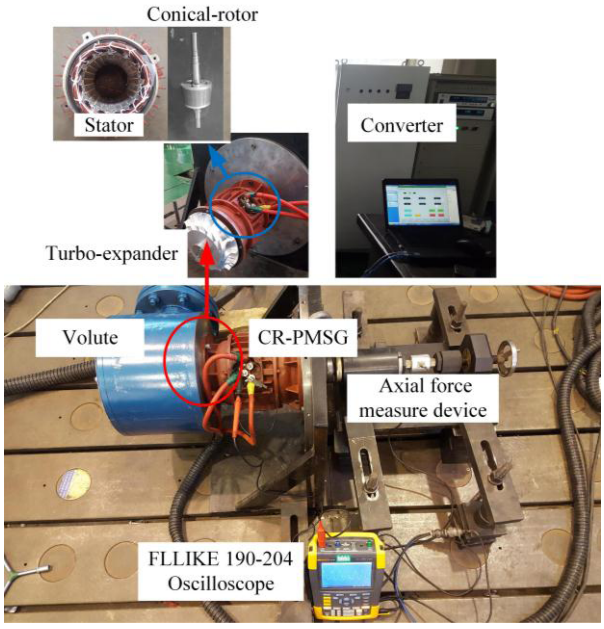

FIGURE 18. Test rig for the CR-PMSG based turbo-expander.

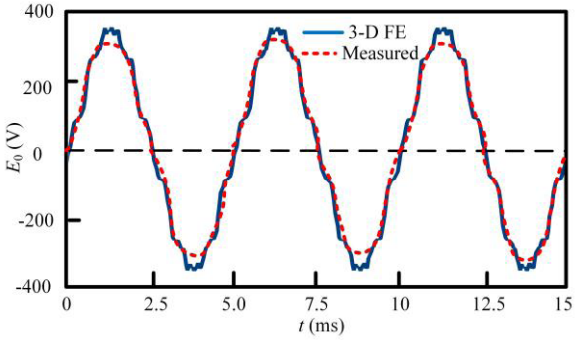

FIGURE 19. Back EMF of the CR-PMSG at no-load condition.

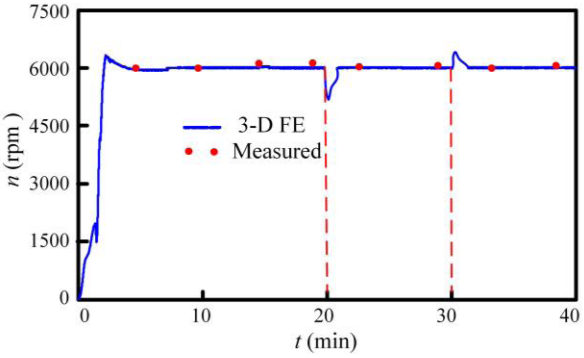

FIGURE 20. Speed response at different load conditions.

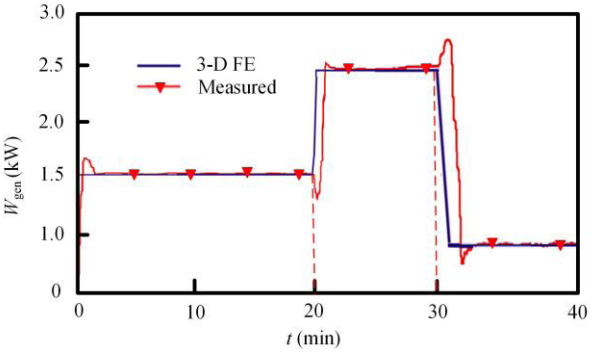

FIGURE 21. Output power at different load conditions.

due to the connection of the shaft and impeller, the rotor of the CR-PMSG will also rotate, converting the mechanical energy into electricity power.

B. ANALYSIS OF TEST RESULTS

The no-load phase back EMF of CR-PMSG is measured and depicted in Fig. 16, of which the RMS value is about 238V. Compared with the 3-D FE simulation result, there is a quite slight difference (about 3%), which confirms the accuracy of FE analysis.

In order to be as close as possible to the actual operation and considering the rotating inertia effect of the power generation system, the switching time of each load conditions in Fig. 15 is changed to $t = 0$, 20min, 30min respectively. The system response to the full load, over load and half load conditions are depicted in Figs.20 -24.

As shown in Fig. 20, the speed response of generator to the applied inlet pressure is quite fast, which starts from 0 to 6000 rpm within 2.0 min. Besides, it is also clear that the speed has a good anti-disturbance performance when there is a pressure change with the load at t=20 min and 30 min.

The output power at different load conditions can be seen in Fig. 21. According to Fig. 8 and Fig. 21, the maximum approximately 92.7 %. Besides, as shown in Fig. 22, the axial force of the turbine impeller is well counteracted by the magnetic axial force generated by the CR-PMSG, and the average value of total axial force is strictly constrained around zero.

The controlled *d, q*-axis currents during the tests are depicted in Fig. 23, which are generally consistent with

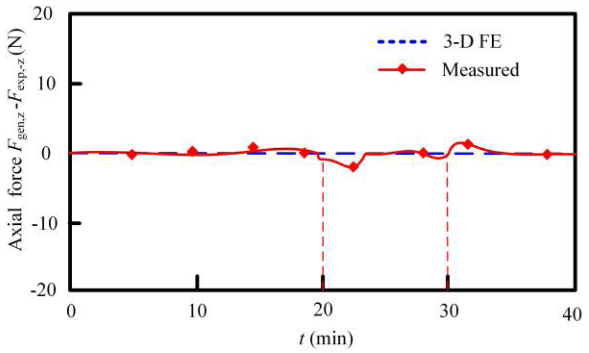

FIGURE 22. The axial force resultant of the CR-PMSG and the turbine impeller at different load conditions.

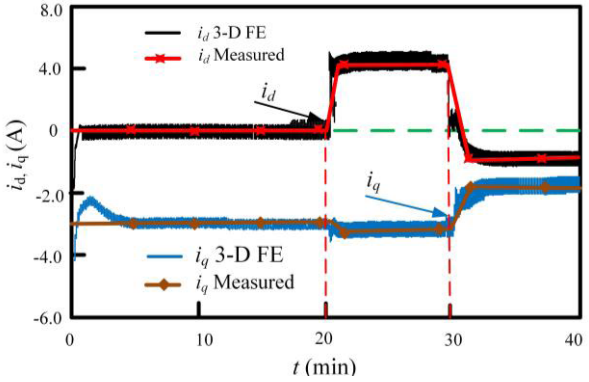

FIGURE 23. *D, q*- axis currents at different load conditions.

the theoretical simulation results. Fig. 24 shows the measured phase current at full load, over load and half load conditions, and the waveform presents a quite good sinusoidal.

The output performance parameters at different load conditions are summarized in Table 3, showing a quite small difference ($\leq$3%) between the measured and 3-D FE results. It is also clear that the axial force ($F_{gen,Z}$-$F_{gen,-Z}$) has a good adaptive equilibrium even if there is a load change, which further confirms the accuracy of the 3-D FE model and analysis.

C. COMPARISON BETWEEN THE PROPOSED CR-PMSG AND CONVENTIONAL PMSG

To make a comparison, a conventional PMSG with the same power and similar geometry is also tested. The proposed CR-PMSG is then compared with the conventional PMSG in terms of torque-speed characteristics.

In practical, the torque coefficient K_A is usually used to represent the effective material per unit volume, which can be expressed by

$$K_A = \frac{S_c}{D_{il}^2 L_{ef} n} \approx 0.166 K_{dp} A B_\delta \times 10^{-3} \quad (13)$$

where, S_c is the apparent power, D_{il} is the inner diameter of stator, and A is the electric load.

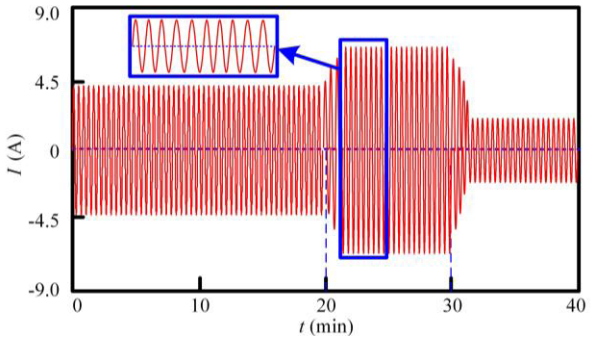

FIGURE 24. Measured phase-A current at different load conditions.

TABLE 3. Parameter comparison between 3-D FE and measured.

Parameter	Symbol	Method	Full load	Over load	Half load
Inlet pressure	$P_{exp,in}$	3-D FEM	121.6 kPa	160.5 kPa	106.2 kPa
		Measured	125.3 kPa	155.6 kPa	108.4 kPa
Outlet pressure	$P_{exp,out}$	3-D FEM	95 kPa	95 kPa	95 kPa
		Measured	101.2 kPa	99.5 kPa	96.2 kPa
Output power	W_{gen}	3-D FEM	1.5 kW	2.5 kW	0.75 kW
		Measured	1.53 kW	2.61 kW	0.72 kW
Output current	I	3-D FEM	3 A (i_d=0, i_q=-3) A	5.4 A (i_d=4.2, i_q=-3.4) A	1.67 A (i_d=-0.5, i_q=-1.6) A
		Measured	3.2 A (i_d=0, i_q=-3.2) A	5.6 A (i_d=4.4, i_q=-3.4) A	1.56 A (i_d=-0.4, i_q=-1.5) A
Axial force	$F_{gen,Z}$ - $F_{exp,-Z}$	3-D FEM	0	0	0
		Measured	-2.1 N	1.3 N	0.9 N

TABLE 4. Parameter comparison between the proposed CR-PMSG and the conventional PMSG.

Parameters	Symbol	Proposed CR-PMSG	Conventional PMSG
Speed	n	6000 rpm	6000 rpm
Outer diameter of stator	$D_{gen,od}$	167 mm	165 mm
Average inner diameter of stator	D_{il}	106.9 mm	107 mm
Length of iron core	L_{ef}	52 mm	50 mm
Apparent power	S_c	2 kVA	2 kVA
Electric load	A	167 A/cm	158 A/cm
Torque coefficient	K_A	0.538 kVA.min/m^3	0.579 kVA.min/m^3

As can be seen in Table 4, both PMSGs have quite similar design dimensions ($D_{gen,od}$, D_{il} and L_{ef}), so they have quite similar K_A, which can also be proved in theory. Thus, the output performance of both machines should be quite similar to each other, which is experimentally confirmed in Fig. 25. According to the operation characteristics of turbo-expander power generation system, it can be seen that with the increase

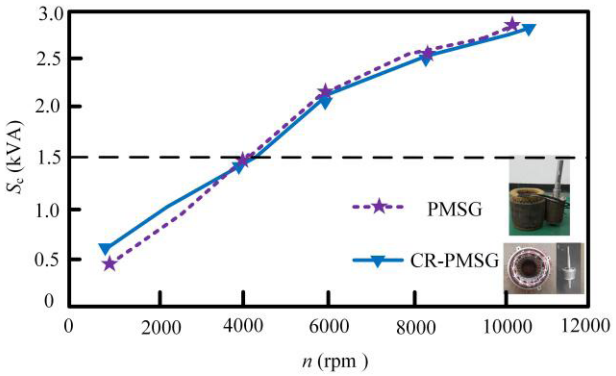

FIGURE 25. Power-speed characteristics of the conventional PMSG and the CR-PMSG.

of output power, the speed of the generator increases, which is similar to that of wind turbine.

V. CONCLUSION

In order to adaptively counteract the axial force of turbine impeller under the high-speed working-fluid impact, a CR-PMSG for high-speed direct-drive turbo-expander has been developed and presented in this paper. Due to its conical-rotor structure, the CR-PMSG can generate an axial magnetic force to balance the axial force of turbine impeller, so the system can be simplified without mechanical balance device. The design method focuses on the analytical procedure and simulation of axial force. The control strategy of *d, q*-axis currents is obtained to achieve the adaptive equilibrium of axial force by 3-D FE simulation, which shows that the *d*-axis current of CR-PMSG plays quite an important role in balancing the axial force produced. The tests results show a good effect of axial force balance and verify the current control strategy. Besides, compared with the conventional PMSG, the proposed machine has the similar material utilization and good output performance. However, it is still quite challenging to derive the expression of axial force with respect to *d, q*-axis currents, as well as to improve the integrated control accuracy of CR-PMSG based turbo-expander system, which will be the priority of future work.

REFERENCES

[1] A. Amiri and M. R. Vaseghi, "Waste heat recovery power generation systems for cement production process," *IEEE Trans. Ind. Appl.*, vol. 51, no. 1, pp. 13–19, Jan./Feb. 2015.

[2] L. Niu *et al.*, "Off-design performance analysis of cryogenic turbo-expander based on mathematic prediction and experiment research," *Appl. Therm. Eng.*, vol. 138, pp. 873–887, Jun. 2018.

[3] V. Minea, "Using geothermal energy and industrial waste heat for power generation," in *Proc. IEEE EPC*, Montreal, QC, Canada, Oct. 2007, pp. 543–549.

[4] E. Sauret and A. S. Rowlands, "Candidate radial-inflow turbines and high-density working fluids for geothermal power systems," *Energy*, vol. 36, no. 7, pp. 4460–4467, Jul. 2011.

[5] H. Guo, Z. Lv, Z. Wu, and B. Wei, "Multi-physics design of a novel turbine permanent magnet generator used for downhole high-pressure high-temperature environment," *IET Electr. Power Appl.*, vol. 7, no. 3, pp. 214–222, May 2013.

[6] S. M. Camporeale, P. D. Ciliberti, B. Fortunato, M. Torresi, A. M. Pantaleo, "Externally fired micro-gas turbine and organic rankine cycle bottoming cycle: Optimal biomass/natural gas combined heat and power generation configuration for residential energy demand," *J. Eng. Gas Turbines Power*, vol. 139, no. 4, p. 041401, Apr. 2017.

[7] F. Mergiotti, F. Crescimbini, L. Solero, and A. Lidozzi, "Design of a turbo-expander driven generator for energy recovery in automotive systems," in *Proc. 19th Int. Conf. Elect. Mach.*, Rome, Italy, Sep. 2010, pp. 1–6.

[8] X.-Y. Wen, L.-C. Zhang, D. Kou, D.-M. Xiao, and H. Zhang, "An adjustment method of axial force on marine multi-shaft gas turbine rotor," in *Proc. ASME Turbo Expo*, Düsseldorf, Germany, 2014, pp. 1–6.

[9] F. Bavassano, M. Mantero, R. Traverso, R. Livermore-Hardy, and B. Blair, "A system integration approach for heavy-duty gas turbine upgrades using improved rotor thrust predictions and application of advanced thrust bearing designs," in *Proc. ASME Turbo Expo*, Charlotte, NC, USA, 2017, pp. 1–10.

[10] S. Sadeghi, H. Saffari, and N. Bahadormanesh, "Optimization of a modified double-turbine Kalina cycle by using artificial bee colony algorithm," *App. Therm. Eng.*, vol. 91, pp. 19–23, Dec. 2015.

[11] S. D. Huang *et al.*, Low-grade thermal energy re-circulation and symmetry double-turbo drive generator power generation system," (in Chinese), ZL Patent 2014 10 697 530.6, Feb. 22, 2017. [Online]. Available: http://www.soopat.com/Patent/201410697530

[12] J. Kurokawa and T. Toykokura, "Study on the axial thrust of the radial flow turbomachinery," in *Proc. 2nd Int. JSME Symp. Fluid Machinery Fluidics*, Tokyo, Japan, 1972, pp. 31–40.

[13] D. Park, S. Heo, H. Cho, and S. Kwon, "Performance evaluation of small-scale liquid pump using a radial turbine with H_2O_2 gas generator," *Trans. Jpn. Soc. Aeronautical Space Sci.*, vol. 58, no. 5, pp. 253–260, 2015.

[14] D. Z. Zhao, E. Winward, Z. Yang, R. Stobart, B. Mason, and T. Steffen, "An integrated framework on characterization, control, and testing of an electrical turbocharger assist," *IEEE Trans. Ind. Electron.*, vol. 65, no. 6, pp. 4897–4908, Jun. 2018.

[15] G. Munteanu, A. Binder, and S. Dewenter, "Five-axis magnetic suspension with two conical air gap bearingless PM synchronous half-motors," in *Proc. SPEEDAM*, Sorrento, Italy, Jun. 2012, pp. 1246–1251.

[16] F. Chai, K. Zhao, Z. Li, and L. Gan, "Flux weakening performance of permanent magnet synchronous motor with a conical rotor," *IEEE Trans. Magn.*, vol. 53, no. 11, Nov. 2017, Art. no. 8208506.

[17] Z.-X. Han and P. G. A. Cizmas, "A CFD method for axial thrust load prediction of centrifugal compressors," *Int. J. Turbo Jet-Engines*, vol. 20, no. 1, pp. 1–16, Apr. 2001.

[18] A. Romagnoli, R. F. Martinez-Botas, and S. Rajoo, "Steady state performance evaluation of variable geometry twin-entry turbine," *Int. J. Heat Fluid Flow*, vol. 32, no. 2, pp. 477–489, Apr. 2011.

[19] B. Guo, Y. Huang, Y. Guo, and J. Zhu, "Thermal analysis of the conical rotor motor using LPTN with accurate heat transfer coefficients," *IEEE Trans. Appl. Supercond.*, vol. 26, no. 7, Oct. 2016, Art. no. 0611507.

[20] H. Qiu, W. Yu, B. Tang, Y. Mu, W. Li, and C. Yang, "Study on the influence of different rotor structures on the axial-radial flux type synchronous machine," *IEEE Trans. Ind. Electron.*, vol. 65, no. 7, pp. 5406–5413, Jul. 2018.

[21] H. Sugimoto, S. Tanaka, A. Chiba, and J. Asama, "Principle of a novel single-drive bearingless motor with cylindrical radial gap," *IEEE Trans. Ind. Appl.*, vol. 51, no. 5, pp. 3696–3706, Sep./Oct. 2015.

[22] K. J. Meessen, J. J. H. Paulides, and E. A. Lomonova, "Force calculations in 3-D cylindrical structures using Fourier analysis and the Maxwell stress tensor," *IEEE Trans. Magn.*, vol. 49, no. 1, pp. 536–545, Jan. 2013.

[23] X. Sun, Z. Xue, J. Zhu, Y. Guo, Z. Yang, and L. Chen, "Suspension force modeling for a bearingless permanent magnet synchronous motor using maxwell stress tensor method," *IEEE Trans. Appl. Supercond.*, vol. 26, no. 7, Oct. 2016, Art. no. 0608705.

[24] R. Dutta and M. F. Rahman, "A comparative analysis of two test methods of measuring $d-$and q-axes inductances of interior permanent-magnet machine," *IEEE Trans. Magn.*, vol. 42, no. 11, pp. 3712–3718, Nov. 2006.

[25] F. Chai, O. Jing, and P. Yulong, "Research on fluxweakening of dual-stator conical permanent magnet synchronous motors," *Trans. China Electro-Tech. Soc.*, vol. 28, no. 7, pp. 12–18, Jul. 2013.

[26] G. Lei, C. Liu, J. Zhu, and Y. Guo, "Techniques for multilevel design optimization of permanent magnet motors," *IEEE Trans. Energy Convers.*, vol. 30, no. 4, pp. 1574–1583, Dec. 2015.

[27] M. T. Jelodar, H. Rastegar, and H. A. Abyaneh, "Modeling turbo-expander systems," *SIMULATION, Trans. Soc. Model. Simul. Int.*, vol. 89, no. 2, pp. 234–248, Feb. 2013.

[28] B. L. J. Gysen, K. J. Meessen, J. J. H. Paulides, and E. A. Lomonova, "General formulation of the electromagnetic field distribution in machines and devices using Fourier analysis," *IEEE Trans. Magn.*, vol. 46, no. 1, pp. 39–52, Jan. 2010.
[29] S. Bozhko, S. Dymko, S. Kovbasa, and S. M. Peresada, "Maximum torque-per-amp control for traction IM drives: Theory and experimental results," *IEEE Trans. Ind. Appl.*, vol. 53, no. 1, pp. 181–193, Jan./Feb. 2017.
[30] E. da Costa Bortoni and J. A. Jardini, "A standstill frequency response method for large salient pole synchronous machines," *IEEE Trans. Energy Convers.*, vol. 19, no. 4, pp. 687–691, Dec. 2004.
[31] Z. Zhu, D. Wu, and X. Ge, "Investigation of voltage distortion in fractional slot interior permanent magnet machines having different slot and pole number combinations," *IEEE Trans. Energy Convers.*, vol. 31, no. 3, pp. 1192–1201, Sep. 2016.

JIAOBAO WANG was born in Hunan, China, in 1981. He received the M.S. degree from Hunan University, Changsha, China, in 2013, where he is currently pursuing the Ph.D. degree with the College of Electrical and Information Engineering. He worked in Xiangtan Electric Manufacturing Co., Ltd., Xiangtan, China, from 2003 to 2010.

His current research interests include electrical machines design and control.

SHOUDAO HUANG (SM'14) was born in Hunan, China, in 1962. He received the B.S. and Ph.D. degrees in electrical engineering from the College of Electrical and Information Engineering, Hunan University, Changsha, China, in 1983, and 2005, respectively.

He is currently a Full Professor with the College of Electrical and Information Engineering, Hunan University.

His research interests include motor design and control, poelectronic system and control, and wind energy conversion system.

CHAO GUO was born in Hunan, China, in 1982. She received the M.S. degree from the Lanzhou University of Technology, Lanzhou, Gansu, China, in 2013. She is currently pursuing the Ph.D. degree with the College of Electrical and Information Engineering, Hunan University, Changsha, China. She worked in Hunan Valin Iron Steel Group Co., Ltd., Xiangtan, China, from 2003 to 2010.

Her current research interests include electrical machines design and control.

HAOKUN WU was born in Hebei, China, in 1995. He received the B.S. degree in electrical engineering from the Hefei University of Technology, Hefei, China, in 2017. He is currently the M.S. degree in electrical engineering with the College of Electrical and Information Engineering, Hunan University, Changsha, China.

His main research interests include high-speed motors and Z-source inverter drive systems.

YAOJING FENG was born in Hunan, China, in 1985. She received the Ph.D. degree in electrical engineering from the Huazhong University of Science and Technology, Wuhan, China, in 2012. She is currently an Assistant Professor of electrical engineering with the College of Electrical and Information Engineering, Hunan University, Changsha, China.

Her main research interests include permanent magnet machines, design and control of electrical motors, and electric vehicle drive systems.